

Continuous dimethyl carbonate synthesis from CO₂ and methanol over Bi_xCe_{1-x}O_δ monoliths: Effect of bismuth doping on population of oxygen vacancies, activity, and reaction pathway

Yongdong Chen¹ (✉), Yue Li¹, Wei Chen¹, Wen Wu Xu² (✉), Zhong-kang Han³, Ammara Waheed⁴, Zhongbin Ye¹, Gao Li⁴ (✉), and Alfons Baiker⁵ (✉)

¹ College of Chemistry and Chemical Engineering, Southwest Petroleum University, Chengdu 610500, China

² School of Physical Science and Technology, Ningbo University, Ningbo 315211, China

³ Center for Energy Science and Technology, Skolkovo Institute of Science and Technology, Skolkovo Innovation Center, Moscow 143026, Russia

⁴ State Key Laboratory of Catalysis, Dalian Institute of Chemical Physics, Chinese Academy of Sciences, Dalian 116023, China

⁵ ETH Zurich, Department of Chemistry and Applied Biosciences, Institute for Chemical and Bioengineering, Hönggerberg, HCI, CH-8093 Zurich, Switzerland

© The Author(s) 2021

Received: 19 March 2021 / Revised: 17 May 2021 / Accepted: 9 June 2021

ABSTRACT

We evaluated bismuth doped cerium oxide catalysts for the continuous synthesis of dimethyl carbonate (DMC) from methanol and carbon dioxide in the absence of a dehydrating agent. Bi_xCe_{1-x}O_δ nanocomposites of various compositions ($x = 0.06-0.24$) were coated on a ceramic honeycomb and their structural and catalytic properties were examined. The incorporation of Bi species into the CeO₂ lattice facilitated controlling of the surface population of oxygen vacancies, which is shown to play a crucial role in the mechanism of this reaction and is an important parameter for the design of ceria-based catalysts. The DMC production rate of the Bi_xCe_{1-x}O_δ catalysts was found to be strongly enhanced with increasing O_v concentration. The concentration of oxygen vacancies exhibited a maximum for Bi_{0.12}Ce_{0.88}O_δ, which afforded the highest DMC production rate. Long-term tests showed stable activity and selectivity of this catalyst over 45 h on-stream at 140 °C and a gas-hourly space velocity of 2,880 mL·g_{cat}⁻¹·h⁻¹. *In-situ* modulation excitation diffuse reflection Fourier transform infrared spectroscopy and first-principle calculations indicate that the DMC synthesis occurs through reaction of a bidentate carbonate intermediate with the activated methoxy (-OCH₃) species. The activation of CO₂ to form the bidentate carbonate intermediate on the oxygen vacancy sites is identified as highest energy barrier in the reaction pathway and thus is likely the rate-determining step.

KEYWORDS

dimethyl carbonate synthesis, bismuth-cerium oxides, monolithic catalyst, oxygen vacancies, reaction mechanism

1 Introduction

Carbon dioxide (CO₂) is a major greenhouse gas, contributing to climate change and global warming [1, 2]. The growing awareness of the detrimental influence of CO₂ in the atmosphere has spurred research on its capture and utilization as a sustainable C1 feedstock for organic syntheses of high value-added chemicals [3]. Prominent examples include the syntheses of methanol [4-7], dimethyl ether (DME) [4, 8], and dimethyl carbonate (DMC) [4, 9-11]. DMC has low toxicity and is non-corrosive, facilitating its safe handling. It is a versatile chemical, which is used for various purposes, such as aprotic polar solvent, methylation and carbonylation agent, intermediate in polycarbonate synthesis, building block in the syntheses of pharmaceuticals, and alternative fuel or oxygenated additive for diesel/gasoline [12-14]. Various methods have been applied for DMC synthesis [9], including transesterification, oxidative carbonylation of methanol, methanolysis of phosgene, and

the direct synthesis of DMC from CO₂ and methanol (CO₂ + 2CH₃OH → CH₃OC(=O)OCH₃ + H₂O). Among these synthetic methods the latter one is considered as an environmentally benign and sustainable green process, as water is the major byproduct [15]. However, inherent problems of this synthetic pathway are the limitation imposed by thermodynamics and the activation of methanol and CO₂. The thermodynamic limitation can be alleviated by applying high CO₂ pressure and most efficiently by rapid removal of the produced water. Consequently, various methods have been explored for the *in-situ* water removal [16], including the use of traps [17], dehydrating agents [18, 19], and membrane reactors [20].

Various types of catalyst have been evaluated for the direct synthesis of DMC from methanol and CO₂ [16], including transition metal oxides and ionic liquids. Among the transition metal oxides ceria-based nanomaterials and mixed oxides have gained particular interest and have shown some potential for the direct DMC synthesis [16, 18, 21-23]. However, the

Address correspondence to Yongdong Chen, yongdongchen@swpu.edu.cn; Wen Wu Xu, xuwenwu@nbn.edu.cn; Gao Li, gaoli@dicp.ac.cn; Alfons Baiker, alfons.baiker@chem.ethz.ch

methanol conversion achieved was mostly below about 13% [24] if no provisions for rapid water removal were taken. The strong beneficial effect of *in-situ* removal of water from the reaction mixture has recently been demonstrated for a ceria catalyst, a high methanol conversion of 95% with ~ 99% DMC selectivity was achieved using a continuous fixed-bed reactor and 2-cyanopyridine as a dehydrating agent [18]. However, the use of a dehydrating agent, such as 2-cyanopyridine, adds considerable complexity to DMC production, because the dehydrating agent has to be recycled and its interaction with reaction components can lead to undesired side reactions. Thus, there remain still two big challenges: the search for highly active and stable catalysts, and efficient practical concepts for the removal of water.

In the present study, we have evaluated various bismuth doped ceria monolithic catalysts, which were coated on a honeycomb ceramic support. To the best of our knowledge Bi-doped ceria has so far not been evaluated as potential catalyst for the direct DMC synthesis [16]. The use of honeycomb-type catalysts could offer several advantages compared to fixed-beds of related particulate catalysts [24–26]. Monolithic catalysts exhibit good interphase mass and heat transfer, low pressure drop at relatively large surface area, and could facilitate more efficient removal of the formed by-product (water), which unfavorably affects the thermodynamic equilibrium and limits the catalytic efficiency of the DMC synthesis [27]. Bismuth trioxide has a cubic fluorite structure like cerium dioxide, and it has been proven that the solid solution of cerium-bismuth could be well formed when the bismuth dopant is present in an appropriate proportion [28]. We synthesized a series of $\text{Bi}_x\text{Ce}_{1-x}\text{O}_\delta$ ($x = 0.06$ to 0.24) nanocomposites with an average particle size in the range of 5.5–7.8 nm and coated them on a ceramic honeycomb. A strong correlation of oxygen vacancies and catalytic performance was observed. Among these monolithic catalysts those based on $\text{Bi}_{0.12}\text{Ce}_{0.88}\text{O}_\delta$ nanocomposite exhibited the best performance in the DMC synthesis, i.e., a promising 20.8% methanol conversion and a high DMC selectivity of 83.5% without using any dehydrating agents. Furthermore, the $\text{Bi}_{0.12}\text{Ce}_{0.88}\text{O}_\delta$ also showed stable catalytic performance over ~ 45 h on stream. *In-situ* modulation excitation spectroscopy in tandem with diffuse reflectance Fourier transform spectroscopy and first-principle calculations were employed to shed some light on the molecular surface processes of the DMC synthesis on this catalyst.

2 Experimental

2.1 Chemicals

All chemicals were used as received. Ammonium ceric nitrate (99.5%, Aladdin), bismuth nitrate (99%, Aladdin), urea (99%, Kelong), glacial acetic acid (99.5%, Kelong), methanol (99.9%, Adamas), CO_2 (99.999%, Jinnengda).

2.2 Preparation of monolithic $\text{Bi}_x\text{Ce}_{1-x}\text{O}_\delta$ catalysts

The $\text{Bi}_x\text{Ce}_{1-x}\text{O}_\delta$ ($0.06 \leq x \leq 0.24$) bimetallic oxides were prepared by an aqueous-phase co-precipitation method [19]. Typically, 15 g $(\text{NH}_4)_2\text{Ce}(\text{NO}_3)_6$ and 1.475 g $\text{Bi}(\text{NO}_3)_3 \cdot 5\text{H}_2\text{O}$ were dissolved in water (500 mL), and 70 g urea in 100 mL aqueous solution was added. This mixture was gradually heated to 90 °C under mechanical stirring (600 rpm) and the formed solution was kept at this temperature for 5 h. Afterward the precipitates were separated by filtration, washed thoroughly with hot water, dried at 80 °C for 12 h, and calcined at 400 °C for another 4 h. The as-prepared Bi-doped cerium oxide powders were then ball-milled with distilled water to form a slurry, which was coated on a cordierite honeycomb (64 cell- cm^{-2} , $\Phi = 10$ mm,

$L = 25$ mm), and the excess slurry was blown off. Finally, the coated cordierite honeycomb was dried at 100 °C and calcined at 400 °C to yield the monolithic catalysts (Fig. 1).

2.3 Characterization

Powder X-ray diffraction (XRD) patterns were recorded on a X'Pert PRO diffractometer (PANalytical) using $\text{Cu-K}\alpha$ radiation of 0.15406 nm at 40 kV and 40 mA to analyze the phase structure of the samples. The XRD data was recorded in the 2θ range of 20° to 80° with a step size of 0.0334° and a counting time of 47 s per step. The results were processed using the Jade-6 software. Raman spectra were recorded at room temperature using a Renishaw inVia spectrometer with a resolution of 2 cm^{-1} . A solid laser beam at 532 nm was used as the exciting source.

N_2 adsorption-desorption isotherms were measured at liquid nitrogen temperature (−196 °C) using an ASAP 2000 instrument (Micromeritics). Before the measurement, the samples were degassed at 300 °C for 3 h. The surface area was determined by multipoint Brunauer-Emmett-Teller analysis of the N_2 -adsorption isotherms.

Transmission electron microscopy (TEM) images were recorded on a Philips FEI Tecnai G² Spirit microscope operated at an accelerating voltage of 120 kV equipped for energy-dispersive X-ray spectroscopy (EDX) analysis. The specimens were prepared by ultrasonically dispersing the sample in ethanol, depositing droplets of the suspensions on a carbon-coated Cu grid, and drying in air.

The Bi-content of the samples was analyzed by inductively coupled plasma atomic emission spectroscopy (ICP-AES) using an Agilent 720ES instrument. The samples of 0.05–0.06 g were dissolved in a 5 mL aqua regia solution with the addition of 30 wt.% H_2O_2 . The as determined bismuth loadings of the $\text{Bi}_x\text{Ce}_{1-x}\text{O}_\delta$ nanocomposites were: 6 wt.%, 12 wt.%, 18 wt.%, and 24 wt.%, respectively.

X-ray photoelectron spectroscopy (XPS) was performed using a Kratos XSAM-800 (UK) spectrometer and $\text{Mg K}\alpha$ radiation at 13 kV and 20 mA. The binding energies were calibrated using the C 1s level (284.8 eV) as an internal reference.

Electron paramagnetic resonance (EPR) spectra were recorded on a Bruker ESP 300e spectrometer. All the samples of 50 mg were pretreated with N_2 (40 $\text{mL}\cdot\text{min}^{-1}$) at 150 °C for 30 min, and then exposed to a flow of argon for 2 h. After pretreatment, the tubular reactor was sealed and transferred to a glove box, where catalysts were loaded into the EPR tubes (Wilma-LabGlass). EPR spectra were recorded in the X-band (9.7 GHz) at room temperature using a microwave power of 20 mW, amplitude modulation of 5 G, and frequency modulation of 100 kHz.

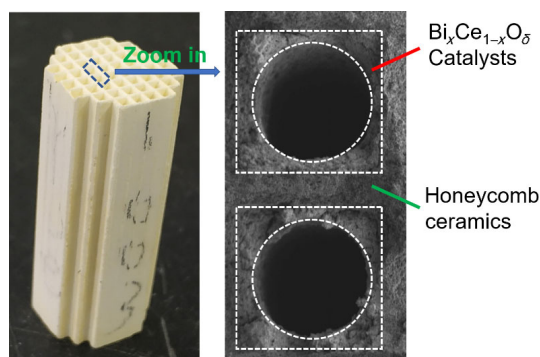


Figure 1 Photograph of ceramic honeycomb monolithic catalysts (left) and SEM image of the cross-sections of the channels of the $\text{Bi}_x\text{Ce}_{1-x}\text{O}_\delta$ monolithic catalysts (right).

Temperature programmed desorption (TPD) of CH₃OH, CO₂, and NH₃ (CH₃OH-, CO₂-, and NH₃-TPD) was performed on a Micromeritics Autochem II Chemisorption Analyzer, connected to a mass spectrometer or a TCD analyzer. 100 mg of catalysts were fixed in a quartz reactor and heated under a He flow of 40 mL·min⁻¹ at 300 °C for 4 hours to remove the adsorbates. Then the sample was cooled to room temperature, saturated with methanol or CO₂, and swept by flowing He overnight. In the TPD measurements the temperature of the samples was ramped to 400 °C at a heating rate of 10 °C·min⁻¹, and the desorbed species were monitored *in-situ* by mass spectrometry (MS) at *m/z* = 31 for the detection of CH₃O-species and at *m/z* = 44 for CO₂ species.

The acidity of the Bi-Ce oxide samples was analyzed by NH₃-TPD. Before measurements the oxides were pretreated at 600 °C in an Ar flow for 1 h and then cooled to room temperature. Subsequently, the sample was exposed to a flow (30 mL·min⁻¹) of 20 vol.% NH₃ balanced with Ar for 0.5 h, followed by exposure to an argon flow until no NH₃ species could be detected anymore. The reactor temperature was programmed to increase at a ramp rate of 10 °C·min⁻¹, and the amount of NH₃ in the effluent was recorded as function of temperature.

2.4 Catalytic test

A pressurized flow-type reaction apparatus with a stainless steel reactor of ~ 11 mm inner diameter was used for the catalytic tests (Scheme S1 in the ESM). The Bi_xCe_{1-x}O_δ and bare CeO₂ monolithic catalysts were evaluated in the DMC synthesis from CH₃OH and CO₂ at 140 °C and 2.4 MPa. Typically, 500 mg of catalysts was coated onto the honeycomb ceramics (2.5 mL) to produce the monolithic catalysts (Fig. 1). Prior to catalytic tests, the reactor was sealed and purged by CO₂ flow for 5 min to remove the air. Then, a mixed gas flow, consisting of a 2:1 molar ratio of CH₃OH (0.145 mL·min⁻¹) and CO₂ (40 mL·min⁻¹) was introduced with a gas hourly space velocity (GHSV) of 2,880 mL·g_{cat}⁻¹·h⁻¹. The product gas mixture was analyzed employing a GC-7890B equipped with a flame ionization detector (FID) through a ten-way valve. The CH₃OH conversion (*X*_{CH₃OH}) and DMC selectivity (*S*_{DMC}) were analyzed when the reactions were at a steady-state. *X*_{CH₃OH} and *S*_{DMC} was calculated as:

$$X_{\text{CH}_3\text{OH}} = \frac{2C_{\text{DMC}} + C_{\text{HCHO}} + 2C_{\text{DME}}}{C_{\text{CH}_3\text{OH}} + 2C_{\text{DME}} + C_{\text{HCHO}} + 2C_{\text{DME}}} \times 100\% \quad (1)$$

$$S_{\text{DMC}} = \frac{C_{\text{DMC}}}{C_{\text{DMC}} + C_{\text{HCHO}} + C_{\text{DME}} + C_{\text{CO}}} \times 100\% \quad (2)$$

Where, *C_i* represents the corresponding component concentration.

2.5 In-situ infrared spectroscopy investigation

Diffuse reflection infrared Fourier transform (DRIFT) spectra were recorded on a Vertex 70v spectrometer (Bruker) equipped with a liquid nitrogen cooled mercury-cadmium-telluride (MCT) detector (ID316, ZnSe Window) and an optical filter (F321). Spectra were recorded at 4 cm⁻¹ spectral resolution and 60 kHz scanning velocity.

Modulation-excitation spectroscopy [29, 30] was carried out by periodically switching between two different gases: (CO₂ → He) and (CH₃OH + CO₂ → He) in two different experiments at 140 and 25 °C. The last five cycles were averaged into one cycle to enhance the *S/N* ratio and time resolution. Phase-sensitive detection [30] was used to further remove the noise and to obtain kinetic information of responding surface species. The phase-domain spectra were obtained via a mathematical

treatment of the time-domain spectra according to the following equation:

$$A_k(\tilde{\nu}) \cos(\varphi_k + \varphi_k^{\text{delay}}(\tilde{\nu})) = \frac{2}{T} \int_0^T A(t, \tilde{\nu}) \sin(k\omega t + \varphi_k) dt$$

where, *T* is the length of a cycle, ω is the demodulation frequency, φ_k is the demodulation phase angle, *k* is the demodulation index (*k* = 1 in this study), and *A*(*t*, $\tilde{\nu}$) and *A_k*($\tilde{\nu}$) are the active species responses in the time and phase domains, respectively.

2.6 First-principle calculations

First-principles calculations were carried out using spin-polarized density functional theory (DFT) with generalized gradient approximation (GGA) of Perdew-Burke-Ernzerhof (PBE) implemented in VASP code [31, 32]. The DFT+U methodology with a value of *U* = 5.0 eV was used in this work, which has been extensively utilized for ceria in the literature [33, 34]. The valence electronic states were expanded in the basis of plane waves with the core-valence interaction represented using the projector augmented wave (PAW) approach and a cutoff of 400 eV [32]. To model the CeO₂(111) surface, a periodic slab with a (5×5) surface unit cell was considered, containing nine atomic layers and a vacuum layer of 15 Å. The bottom three atomic layers of ceria substrate were fixed to mimic the bulk structure, whereas the other layers were allowed to relax during geometry optimizations. Due to the large supercell, *k*-point sampling was restricted to Γ point. (2×2×1) *k*-points were also used to validate our results. The climbing image nudged elastic band (CI-NEB) method was used for the transition state calculations [35]. The Gibbs adsorption free energy (ΔG) was calculated according to $\Delta G = \Delta E + \Delta \text{ZPE} - T\Delta S$, and the zero point energy (ZPE) for the adsorbed species by using the finite-displacement method with the fixed substrate. The entropy corrections for the adsorbates on the surface were considered zero, since the main contribution to the entropy is due to the translational entropy.

3 Results and discussion

3.1 Characterization of Bi_xCe_{1-x}O_δ nanocomposites

XRD patterns of the series of Bi_xCe_{1-x}O_δ (*x* = 0.06 to 0.24) nanocomposites prepared by the described coprecipitation method are shown in Fig. 2(a). The pure CeO₂ particles exhibit intense diffraction peaks at 28.4°, 33.0°, 47.4°, and 56.3° for the (111), (200), (220), and (311) faces of the cubic fluorite structure of CeO₂ (PDF#43-1002), respectively. Notably, no diffraction line indicative of isolated Bi₂O₃ oxide was observed, implying that the Bi species were well-dispersed in the lattice

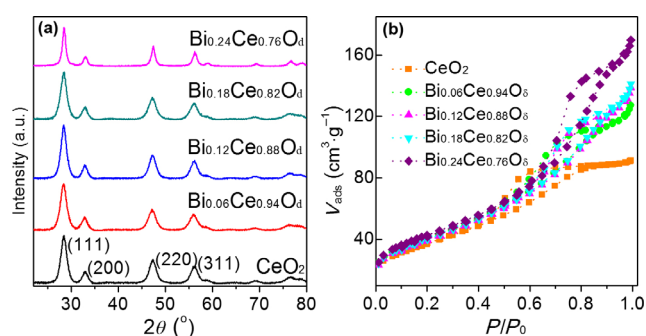


Figure 2 Characterization of the Bi_xCe_{1-x}O_δ nanocomposites: (a) XRD patterns, (b) N₂ adsorption-desorption isotherms. The corresponding BET surface areas (m²·g⁻¹) are: CeO₂, 134; Bi_{0.06}Ce_{0.94}O_δ, 148; Bi_{0.12}Ce_{0.88}O_δ, 145; Bi_{0.18}Ce_{0.82}O_δ, 149, and Bi_{0.24}Ce_{0.76}O_δ, 155.

of CeO₂. Compared with the diffraction pattern of pure CeO₂, the intensity of the Bi_xCe_{1-x}O_δ reflections gradually weakened with increasing concentration of Bi species and the reflection angle of the (111) facet shifted from 28.580° (for CeO₂) to 28.786° (Bi_xCe_{1-x}O_δ). Correspondingly, the lattice parameter gradually increased from 0.5418 nm (in CeO₂) to 0.5441 nm (Bi_{0.24}Ce_{0.76}O_δ), corroborating that the Bi species were successfully incorporated into the CeO₂ lattice forming a solid solution.

Structural properties of the Bi_xCe_{1-x}O_δ nanocomposites are summarized in Table 1. Figure 2(b) shows the N₂-adsorption-desorption isotherms of the Bi_xCe_{1-x}O_δ samples. All samples showed Type IV isotherms. The N₂-uptake increased with higher Bi content of the nanocomposites, as also reflected by the increasing BET surface areas (Table 1). The surface properties of the Bi_xCe_{1-x}O_δ nanocomposites were investigated by Raman spectroscopy, EPR, TEM, EDX, XPS, and TPD of CO₂, CH₃OH, and NH₃.

The concentration of oxygen vacancies (O_v) was analysed using Raman spectroscopy, EPR, and XPS. Figure 3(a) shows the Raman spectra of the different nanocomposites. Two distinct Raman bands appeared at 465 and 600 cm⁻¹. The band at 465 cm⁻¹ represents the symmetrical stretching F_{2g} mode of Ce-O [36]. The F_{2g} band was broadened and slightly shifted to higher wave numbers when the Bi³⁺ species were incorporated into the ceria lattice forming Bi_xCe_{1-x}O_δ bimetallic oxides. The O_v concentrations derived by evaluating the Raman spectra are presented in the ESM.

Figure 3(b) depicts the EPR spectra of CeO₂ and the Bi_{0.12}Ce_{0.88}O_δ nanocomposite, typical for the Bi_xCe_{1-x}O_δ oxides. An intensive single line EPR signal with *g* ≈ 2.003 was observed with both CeO₂ and the Bi_{0.12}Ce_{0.88}O_δ nanocomposite, indicating the presence of surface Ce³⁺ with free electrons and oxygen vacancies [37]. Note that Bi_{0.12}Ce_{0.88}O_δ showed a stronger EPR signal compared to CeO₂, indicating a much higher O_v concentration, in line with XPS results (Table 1) and the Raman results presented in the ESM.

TEM images of the Bi_xCe_{1-x}O_δ oxides are shown in Fig. 4. The average crystal sizes of the samples with different composition were: Bi_{0.06}Ce_{0.94}O_δ (~ 8.9 nm), Bi_{0.12}Ce_{0.88}O_δ (~ 6.5 nm), Bi_{0.18}Ce_{0.82}O_δ (~ 6.3 nm), and Bi_{0.24}Ce_{0.76}O_δ (~ 6.1 nm). The decreasing particle size with higher concentration of Bi species indicates that the crystal growth of the oxide particles was inhibited due to the lattice expansion generated by the incorporation of Bi (Bi³⁺ cation radius (0.103 nm) is larger than that of the Ce⁴⁺ cation (0.087 nm)). EDX elemental mapping confirmed that Bi species were uniformly dispersed in the ceria forming bimetal oxides, as representatively shown for the Bi_{0.12}Ce_{0.88}O_δ nanocomposite in Fig. 5.

Next, the chemical states and oxygen vacancies of Bi_xCe_{1-x}O_δ

were investigated using XPS. The Ce 3d spectra (Fig. 6(a)) shows characteristic peaks of v, v', and v'', corresponding to Ce 3d_{5/2}, which are assigned to Ce⁴⁺ ions in Bi_xCe_{1-x}O_δ. The peaks of v₀ and v' belong to the Ce 3d_{5/2} of Ce³⁺ species [38]. While some Ce³⁺ species were also present in the bare CeO₂ samples, the concentration of Ce³⁺ in Bi_xCe_{1-x}O_δ was significantly higher, ranging from 16.1% to 20.8% (Table 1). This indicates that some Ce⁴⁺ was reduced to Ce³⁺ when Bi³⁺ ions were introduced into the ceria lattice. Bismuth was present as Bi³⁺ species, as indicated by the XPS analyses presented in Fig. S3 in the ESM [28].

The O 1s spectra are shown in Fig. 6(b). The asymmetric spectra can be deconvoluted into three peaks with BEs of ~ 529.3, 530.5, and 532.2 eV, respectively. These BEs have been associated to O²⁻ species in the lattice (O_L), oxygen vacancies or defects (O_v), and chemisorbed or dissociated oxygen species, such as hydroxyl groups (O_H), respectively [39–42]. The oxygen vacancy (O_v) concentrations estimated from these spectra are listed in Table 1. The concentration of O_v in ceria (23.2%) increased strongly with incorporation of Bi³⁺ into the ceria lattice and reached a maximum of 37.3% in Bi_{0.12}Ce_{0.88}O_δ, in accord with the strong EPR signal observed with this sample (Fig. 3(b)).

3.2 Catalytic performance in DMC synthesis

The catalytic performance of the Bi_xCe_{1-x}O_δ catalysts, coated on the honeycomb ceramics, were evaluated for the DMC synthesis. The reactions were carried out at a pressure of 2.4 MPa [24–26]. The results of the catalytic tests are presented in Fig. 7. Note that beside the main reaction (DMC synthesis), the formation of DME 2CH₃OH → CH₃OCH₃ + H₂O, formaldehyde CH₃OH + CO₂ → HCHO + CO + H₂O, and methanol decomposition CH₃OH + 2CO₂ → 3CO + 2H₂O were observed [15]. The catalytic performance over the best catalyst, Bi_{0.12}Ce_{0.88}O_δ, was evaluated at different reaction temperatures from 100 to 180 °C. Figure 7(a) shows that the methanol conversion reached a maximum at around 160 °C, while the selectivity to S_{DMC} decreased monotonically with increasing temperature in the investigated temperature range. The optimal reaction temperature for the production of DMC was around 140 °C, taking into account both methanol conversion and DMC selectivity. In Fig. 7(b) the catalytic performances of the Bi_xCe_{1-x}O_δ catalysts with different Bi-content (*x*) are compared.

The curve of CH₃OH conversion shows a distinct maximum for the Bi_{0.12}Ce_{0.88}O_δ catalyst (dashed black line). This nanocomposite exhibited the highest activity (~ 21% conversion of CH₃OH), while, the DMC selectivity gradually decreased from 89% to 72% with increasing concentration of incorporated bismuth. Taken all together, the Bi_{0.12}Ce_{0.88}O_δ afforded the

Table 1 Structural and chemical properties of Bi_xCe_{1-x}O_δ nanocomposites

Oxides	(111) plane		Lattice parameter (nm) ^a	Average crystal size (nm) ^b	Acidity NH ₃ uptake (cm ³ ·NH ₃ ·g _{cat} ⁻¹) ^c	Conc. of Ce ³⁺ (%) ^d	Conc. of O _v (%) ^d
	2θ (°)	<i>d</i> (nm)					
Bare CeO ₂	28.510	0.3128	0.5418	10.3	64.7	16.1	23.2
Bi _{0.06} Ce _{0.94} O _δ	28.511	0.3128	0.5429	8.9	62.0	18.0	34.8
Bi _{0.12} Ce _{0.88} O _δ	28.611	0.3139	0.5434	6.5	60.3	20.8	37.3
Bi _{0.18} Ce _{0.82} O _δ	28.644	0.3135	0.5438	6.3	57.4	19.1	32.1
Bi _{0.24} Ce _{0.76} O _δ	28.786	0.3142	0.5441	6.1	52.9	17.7	30.1

^aLattice parameter calculated according to Vegard's law; ^bCrystal size of the oxide nanocomposites determined by TEM; ^cDetermined by NH₃-TPD.

^dConcentration of Ce³⁺ and O_v estimated from XPS data. The O_v concentrations were estimated from the integrated peak areas, where A_{OL}, A_{OV} and

A_{OH} represent the photoelectron peak areas of O_L, O_v and O_H, respectively (Eq. (3)): $[O_v] \% = \frac{A_{OV}}{A_{OV} + A_{OL} + A_{OH}} \times 100\%$.

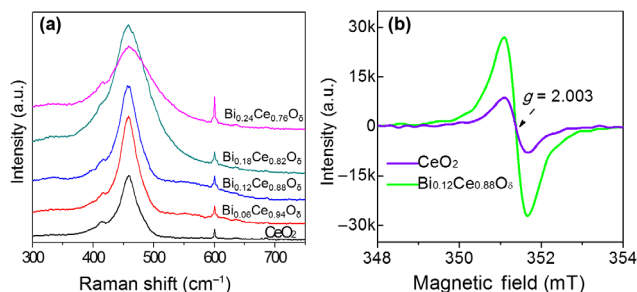


Figure 3 (a) Raman spectra and (b) typical EPR spectrum of $\text{Bi}_x\text{Ce}_{1-x}\text{O}_\delta$ nanocomposites compared to corresponding spectrum of CeO_2 .

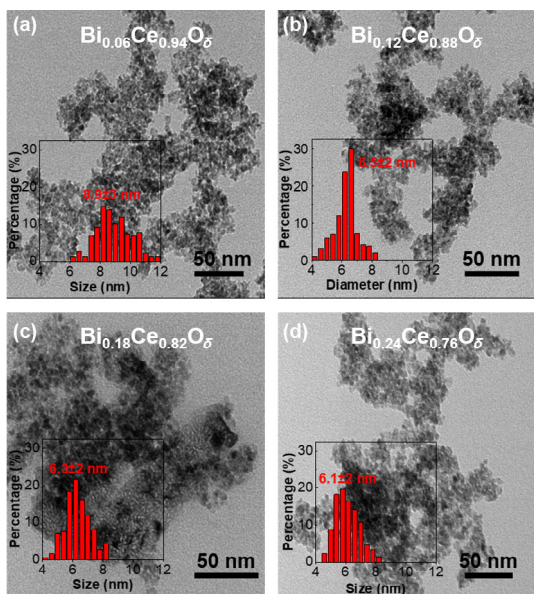


Figure 4 (a)–(d) TEM images of $\text{Bi}_x\text{Ce}_{1-x}\text{O}_\delta$ nanocomposites and corresponding histograms of particle size distributions. Approximately 300 particles were randomly counted for each sample.

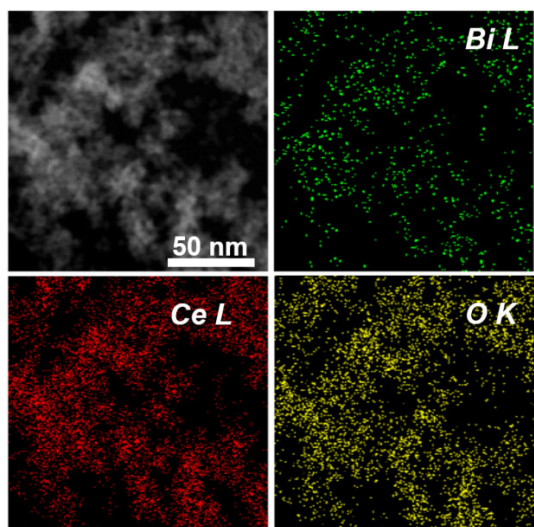


Figure 5 TEM image (top left) and corresponding element mapping by EDX of $\text{Bi}_{0.12}\text{Ce}_{0.88}\text{O}_\delta$ nanocomposite. Further images are presented in Figs. S1 and S2 in the ESM.

best catalytic performance (highest yield of DMC), including CH_3OH conversion and DMC selectivity, which is mainly due to its surface properties (*vide infra*). The cordierite support without Bi-Ce oxide coating was inactive for the DMC synthesis under identical reaction conditions, corroborating that the catalytic active sites are associated with the Bi-Ce oxides.

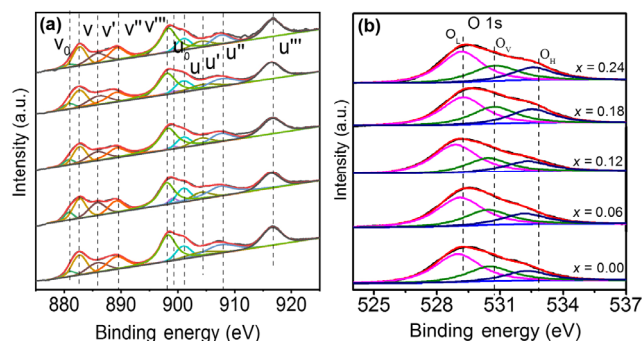


Figure 6 XPS analyses of $\text{Bi}_x\text{Ce}_{1-x}\text{O}_\delta$ nanocomposites. (a) Ce 3d spectra, and (b) O 1s spectra. x refers to mole fraction of Bi in the $\text{Bi}_x\text{Ce}_{1-x}\text{O}_\delta$ samples.

Further, we examined the relationship between the catalytic activity and concentration of oxygen vacancies. Figure 7(c) shows that the DMC productivity of the $\text{Bi}_x\text{Ce}_{1-x}\text{O}_\delta$ catalysts is strongly enhanced with increasing O_v concentration. Although the exact determination of the O_v concentration by XPS may be subject to some uncertainty, there is no doubt that higher O_v concentrations result in higher DMC productivity, as Raman and EPR investigations further substantiated. These results clearly indicate that oxygen vacancies play a crucial role in the catalytic process.

In DMC synthesis often deactivation of catalysts caused by the accumulation of carbonate species (e.g., CO_3^{2-}) on the catalyst surface has been reported [8]. Therefore, we also investigated the long-term behavior of the best performing catalyst, $\text{Bi}_{0.12}\text{Ce}_{0.88}\text{O}_\delta$, under identical reaction conditions. As shown in Fig. 8, the CH_3OH conversion and selectivity to DMC remained stable at $20.6 \pm 0.3\%$ and $85.1 \pm 1\%$, respectively, over the test duration of 45 h on stream. The DMC formation rate on $\text{Bi}_{0.12}\text{Ce}_{0.88}\text{O}_\delta$ reached up to $\sim 40 \text{ mmol DMC} \cdot \text{g}_{\text{cat}}^{-1} \cdot \text{h}^{-1}$. Thus, the Bi-doped cerium oxide monolithic catalyst exhibited excellent stability in the continuous DMC synthesis, which is mainly due to the robust nature of the Bi-doped cerium oxides, as evidenced by the XRD and TEM analyses of the spent $\text{Bi}_{0.12}\text{Ce}_{0.88}\text{O}_\delta$ catalyst after the long-term tests, Figs. S4 and S5 in the ESM.

3.3 CO_2 - and CH_3OH -TPD

TPD was applied to study the adsorption properties of the $\text{Bi}_{0.12}\text{Ce}_{0.88}\text{O}_\delta$ nanocomposite for methanol and carbon dioxide [39, 43]. As shown in Fig. 9(a), a broad desorption peak ranging from ~ 70 to ~ 200 °C was observed in the CO_2 -TPD, which is attributed to the removal of bidentate carbonate species on the oxide surface [44].

Note that the intensity of the desorption peak of the $\text{Bi}_{0.12}\text{Ce}_{0.88}\text{O}_\delta$ nanocomposite is much higher than that of bare CeO_2 , indicating that CO_2 adsorption is enhanced on $\text{Bi}_{0.12}\text{Ce}_{0.88}\text{O}_\delta$, which exhibits a much higher concentration of oxygen vacancies than bare ceria (cf. Table 1). The CH_3OH desorption profiles in (Fig. 9(b)) show two peaks centered at ~ 100 and 300 °C, which are assigned to associative and dissociative adsorption (CH_3O^-) of CH_3OH , respectively [39]. Interestingly, the intensity of the latter peaks is similar, implying that the stability of methanol chemisorbed on $\text{Bi}_{0.12}\text{Ce}_{0.88}\text{O}_\delta$ and bare CeO_2 is similar. The TPD results indicate that the Bi-doping strongly enhances the CO_2 adsorption uptake of ceria and that the activation of carbon dioxide plays a crucial role in the dimethyl carbonate synthesis from CO_2 and CH_3OH (*vide infra*).

The NH_3 -TPD analyses showed that the acidic properties

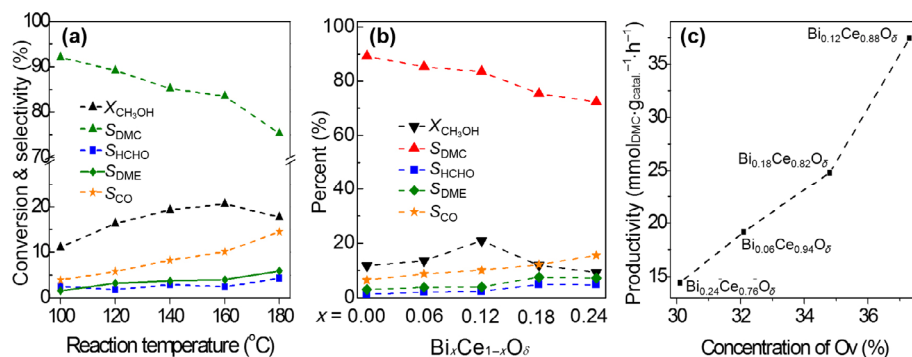


Figure 7 (a) Catalytic performance of best performing catalyst $\text{Bi}_{0.12}\text{Ce}_{0.88}\text{O}_\delta$ in DMC synthesis from CH_3OH and CO_2 . (b) Catalytic performance over the different $\text{Bi}_x\text{Ce}_{1-x}\text{O}_\delta$ nanocomposites as a function of the Bi content (x). Reaction conditions: 500 mg catalysts, GHSV of $2,880 \text{ mL}\cdot\text{g}_{\text{cat}}^{-1}\cdot\text{h}^{-1}$, stoichiometric ratio of CH_3OH : CO_2 is 2:1 (mol/mol), 2.4 MPa, at 140°C . (c) DMC productivity over the $\text{Bi}_x\text{Ce}_{1-x}\text{O}_\delta$ catalysts as a function of the concentration of oxygen vacancies (O_v).

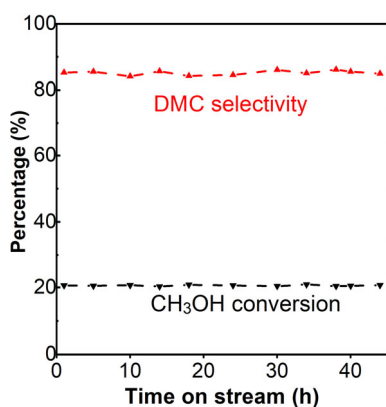


Figure 8 Long-term stability of $\text{Bi}_{0.12}\text{Ce}_{0.88}\text{O}_\delta$ monolithic catalyst over $\sim 45 \text{ h}$ on-stream. Reaction conditions: 500 mg catalysts, GHSV of $2,880 \text{ mL}\cdot\text{g}_{\text{cat}}^{-1}\cdot\text{h}^{-1}$, stoichiometric ratio of CH_3OH : CO_2 2:1 (mol/mol), $p = 2.4 \text{ MPa}$, and 140°C .

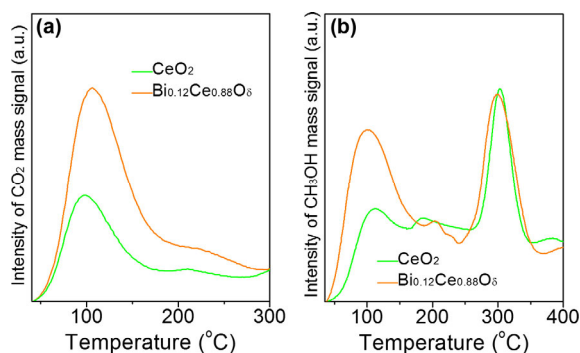


Figure 9 (a) Temperature programmed desorption (TPD) of CO_2 (m/z 44) and (b) CH_3OH (m/z 31) on $\text{Bi}_{0.12}\text{Ce}_{0.88}\text{O}_\delta$ composite and CeO_2 . Sample mass, 100 mg; heating rate, $10^\circ\text{C}\cdot\text{min}^{-1}$.

of the oxides slightly decreased with increasing concentration of the bismuth dopant (Table 1 and Table S1 in the ESM). However, no obvious correlation between acidic properties and catalytic performance was observed.

3.4 *In-situ* infrared spectroscopy

To gain deeper insight into the species formed on the catalyst surface, we carried out *in-situ* DRIFTS studies coupled with modulation excitation spectroscopy and phase sensitivity detection at the reaction temperature of 140°C [29, 30]. In the first experiments (Fig. 10(a)), periodically switching between CO and He ($\text{CO}_2 \rightarrow \text{He}$ modulation) was applied. The main species adsorbed on the surface of the catalyst were carbonate and bidentate carbonate species. The IR bands at $1,018 \text{ cm}^{-1}$

are assigned to the C–O bond of bidentate carbonate species [44]. The IR bands at $1,539$ and $1,392 \text{ cm}^{-1}$ are attributed to “O–C–O” of bidentate carbonate species. The formation of the bidentate carbonate species involved surface hydroxyl groups (–OH), as the broad band at $1,269 \text{ cm}^{-1}$ belongs to CO–H of bidentate carbonate species [45]. The bidentate carbonate also shows a broad band at $1,634 \text{ cm}^{-1}$ [46]. Therefore, the bidentate carbonate species should be formed when CO_2 adsorbed on the oxygen vacancy sites through insertion of one O atom into the vacancy site on the catalyst surface. Of note, bands due to the physically adsorbed CO_2 appeared at $\sim 2,359$ and $2,343 \text{ cm}^{-1}$ [47]. As a side-product formate species were also detected. The newly appearing positive bands at $2,900$, $2,858$ and $2,855 \text{ cm}^{-1}$, combined with the negative going bands at 949 and $1,018 \text{ cm}^{-1}$, indicate the cleavage of the O–C bond of carbonate, promoting the formation of formate species [48].

Next, the *in-situ* DRIFTS monitoring was carried out by periodically switching between the reactant gas mixture and He ($\text{CH}_3\text{OH} + \text{CO}_2 \rightarrow \text{He}$), Fig. 10(b). The introduction of the reactant gas mixture gave rise to the appearance of bands at

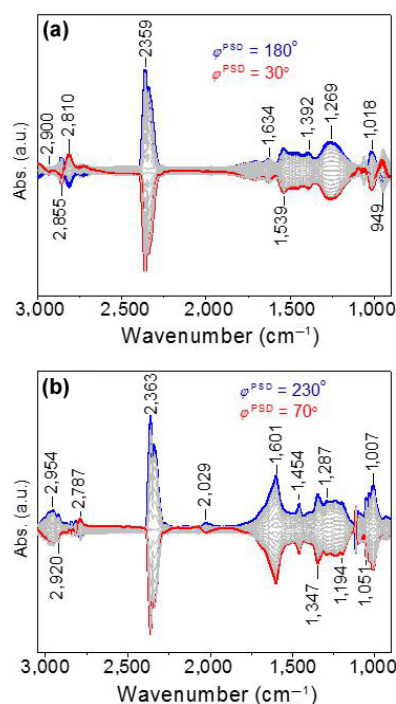


Figure 10 Phase-domain DRIFT spectra during: (a) CO_2 adsorption (switching between $\text{CO}_2 \leftrightarrow \text{He}$ at 25°C . and (b) (switching between $\text{CH}_3\text{OH} + \text{CO}_2 \leftrightarrow \text{He}$ at 140°C) over $\text{Bi}_{0.12}\text{Ce}_{0.88}\text{O}_\delta$. The formed and consumed species emerge as positive and negative IR bands, respectively.

1,194, 1,051, and 1,007 cm^{-1} , which are assigned to the C–O stretching modes of terminal (*t*-OCH₃) and bridged (*b*-OCH₃) methoxy species, respectively [49]. Furthermore, the newly appearing positive bands at 1,601, 1,456, 1,347 and 1,287 cm^{-1} indicate the production of the monodentate methyl carbonate species (CH₃O-C(=O)-O) [49]. The methyl carbonate quickly reacted with the activated methoxy species to yield the final product DMC, as the observation of a drastic decrease of methoxy species at 1,007 cm^{-1} and the simultaneously increasing band at 1,601 cm^{-1} indicates [44].

3.5 Theoretical consideration of the reaction mechanism

To gain further insight into the reaction mechanism, the reaction paths of the DMC synthesis from CO₂ and CH₃OH on the Bi-doped reduced ceria surface were investigated by first-principle calculations. The decreased average oxygen vacancy formation energy with increasing Bi-doping of ceria was examined, as shown in Fig. 11. The results show that doping of ceria with Bi atoms can enhance the formation of oxygen vacancies, which is consistent with the experimental observations.

The reaction pathway proposed based on the experimental and theoretical results is presented in Fig. 12. Two energetically feasible reaction pathways are shown. The adsorption of CH₃OH on the Bi-doped reduced ceria surface can generate a reaction Gibbs free energy (ΔG) of -0.76 eV, suggesting this surface can facilitate the adsorption of CH₃OH, as corroborated by the CH₃OH-TPD measurements shown in Fig. 9(b).

The adsorbed CH₃OH can dissociate to methoxy species via subtraction of a proton (path 1). This dissociation has to overcome a small energy barrier of 0.18 eV and generates -0.41 eV reaction energy, indicating that it can easily occur. The formed methoxy species can refill an oxygen vacancy on the surface. The following adsorption of CO₂ will refill another oxygen vacancy. CO₂ is prone to adsorb perpendicular to the surface. Then the adsorbed methoxy and CO₂ react together to form the monodentate methyl carbonate (CH₃O-C(=O)-O, path 1). This is the first potential rate-determining step, which needs to overcome an energy barrier of 0.84 eV.

Alternatively, the monodentate methyl carbonate can also be directly formed from the adsorbed CH₃OH and CO₂ by overcoming an energy barrier of 0.69 eV (path 2). The monodentate methyl carbonate can directly react with the second adsorbed CH₃OH to give the final DMC product. This process is the second potential rate determining step and needs to overcome an energy barrier of 0.98 eV. Finally, the DMC

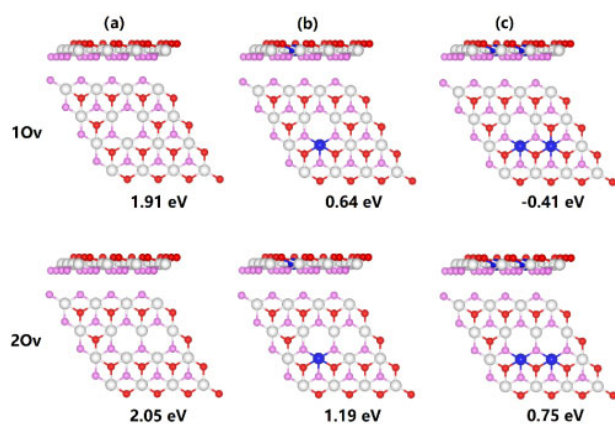


Figure 11 Average oxygen vacancy (O_v) formation energies. Only the top three atomic layers are shown for clear demonstration. Cerium, surface oxygen, subsurface oxygen, and Bi atoms are in white, red, pink, and blue, respectively.

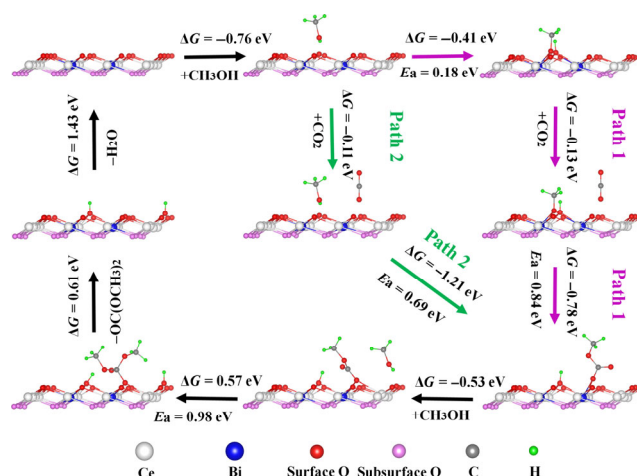


Figure 12 Proposed reaction pathways at Bi doped reduced ceria surfaces. Only the top three atomic layers are shown for clear demonstration. Cerium, surface oxygen, subsurface oxygen, Bi, C, and H atoms are in white, red, pink, blue, grey, and green, respectively. E_a represents the energy barrier.

and H₂O products will desorb from the surface.

It is interesting to compare the reaction paths proposed here, based on *in-situ* DRIFTS, TPD, and theoretical calculations for the DMC synthesis over the Bi-doped ceria with that earlier suggested by Marin et al. [10] for this reaction over ceria nanorods and commercial ceria. Based on initial reaction rate data, they derived a reaction rate law where the order with respect to ceria and CO₂ was approximately +1, and that of CH₃OH -1 . This finding indicates that over ceria the reaction obeys Langmuir-Hinshelwood kinetics, where CO₂ and CH₃OH are binding to the catalyst surface in separate steps and implies that CO₂ adsorption and activation is the rate-determining step. This scenario is in line with reaction path 1 in Fig. 12, indicating that the reaction paths is similar on Bi_xCe_{1-x}O_δ and ceria. However, based on the theoretical calculations direct DMC production via reaction path 2 is energetically also feasible.

4 Conclusions

Bismuth doped Bi_xCe_{1-x}O_δ nanocomposites with different Bi content were coated on a ceramic honeycomb and their catalytic properties were evaluated in the continuous synthesis of DMC from CO₂ and CH₃OH in the absence of any dehydrating agent. The Bi_xCe_{1-x}O_δ nanocomposites were synthesized by an aqueous-phase co-precipitation method and characterized by XRD, TEM, EDX, EPR, XPS, TPD, and DRIFTS. The population of oxygen vacancies in the Bi_xCe_{1-x}O_δ nanocomposites was found to depend on the concentration of the Bi dopant and proved to be crucial for this reaction. The DMC production rate over the Bi_xCe_{1-x}O_δ nanocomposites increased with higher oxygen vacancies (O_v) concentration, reaching a maximum for Bi_{0.12}Ce_{0.88}O_δ. *In-situ* DRIFTS combined with modulation excitation spectroscopy and first-principle calculations suggest that DMC is formed via coupling of bidentate carbonate species with the activated methoxy species on the surface of these catalysts. The catalytic performance of Bi_{0.12}Ce_{0.88}O_δ is among the best achieved so far with ceria-based catalysts in the absence of a dehydrating agent. The performance of the Bi_{0.12}Ce_{0.88}O_δ catalyst was stable in long-term tests over 45 h on-stream. However, as with other catalysts, economic production of DMC can only be achieved if the thermodynamic limitation is overcome by *in-situ* removal of the water formed as by-product.

Acknowledgements

We acknowledged the financial supported by the National Natural Science Foundation of China (Nos. 21773189 and 11974195) and Department of Science and Technology of Sichuan Province (19ZDZX0113) and Liaoning Revitalization Talents Program (XLYC1807121).

Electronic Supplementary Material: Supplementary material (schematic diagram of reactor module, TEM images, element mapping, Bi 4f XPS spectra of $\text{Bi}_x\text{Ce}_{1-x}\text{O}_8$ nanoparticles, NH_3 -TPD, and Raman spectroscopy data) is available in the online version of this article at <https://doi.org/10.1007/s12274-021-3669-4>.

Funding note: Open access funding provided by Swiss Federal Institute of Technology Zurich.

Open Access This article is licensed under a Creative Commons Attribution 4.0 International License, which permits use, sharing, adaptation, distribution and reproduction in any medium or format, as long as you give appropriate credit to the original author(s) and the source, provide a link to the Creative Commons licence, and indicate if changes were made.

The images or other third party material in this article are included in the article's Creative Commons licence, unless indicated otherwise in a credit line to the material. If material is not included in the article's Creative Commons licence and your intended use is not permitted by statutory regulation or exceeds the permitted use, you will need to obtain permission directly from the copyright holder.

To view a copy of this licence, visit <http://creativecommons.org/licenses/by/4.0/>.

References

- [1] Souza, L. F. S.; Ferreira, P. R. R.; de Medeiros, J. L.; Alves, R. M. B.; Araújo, O. Q. F. Production of DMC from CO_2 via indirect route: Technical-economical-environmental assessment and analysis. *ACS Sustain. Chem. Eng.* **2014**, *2*, 62–69.
- [2] Albrecht, M.; Rodemerck, U.; Schneider, M.; Bröring, M.; Baabe, D.; Kondratenko, E. V. Unexpectedly efficient CO_2 hydrogenation to higher hydrocarbons over non-doped Fe_2O_3 . *Appl. Catal. B: Environ.* **2017**, *204*, 119–126.
- [3] Modak, A.; Bhanja, P.; Dutta, S.; Chowdhury, B.; Bhaumik, A. Catalytic reduction of CO_2 into fuels and fine chemicals. *Green Chem.* **2020**, *22*, 4002–4033.
- [4] Wu, J. J.; Zhou, X. D. Catalytic conversion of CO_2 to value added fuels: Current status, challenges, and future directions. *Chin. J. Catal.* **2016**, *37*, 999–1015.
- [5] Kuan, C.; Wang, T. F.; Chen, J. G. Hydrogenation of CO_2 to methanol over CuCeTiO_x catalysts. *Appl. Catal. B: Environ.* **2017**, *206*, 704–711.
- [6] Mou, S. Y.; Wu, T. W.; Xie, J. F.; Zhang, Y.; Ji, L.; Huang, H.; Wang, T.; Luo, Y. L.; Xiong, X. L.; Tang, B. et al. Boron phosphide nanoparticles: A nonmetal catalyst for high-selectivity electrochemical reduction of CO_2 to CH_3OH . *Adv. Mater.* **2019**, *31*, 1903499.
- [7] Zhang, Y. J.; Li, D. B.; Zhang, Y.; Cao, Y.; Zhang, S. J.; Wang, K. J.; Ding, F.; Wu, J. V-modified $\text{CuO-ZnO-ZrO}_2/\text{HZSM-5}$ catalyst for efficient direct synthesis of DME from CO_2 hydrogenation. *Catal. Common.* **2014**, *55*, 49–52.
- [8] Owen, R. E.; Plucinski, P.; Mattia, D.; Torrente-Murciano, L.; Ting, V. P.; Jones, M. D. Effect of support of Co-Na-Mo catalysts on the direct conversion of CO_2 to hydrocarbons. *J. CO₂ Util.* **2016**, *16*, 97–103.
- [9] Keller, N.; Rebmann, G.; Keller, V. Catalysts, mechanisms and industrial processes for the dimethylcarbonate synthesis. *J. Mol. Catal. A: Chem.* **2010**, *317*, 1–18.
- [10] Marin, C. M.; Li, A.; Bhalkikar, L.; Doyle, J. E.; Zeng, X. C.; Cheung,

- C. L. Kinetic and mechanistic investigations of the direct synthesis of dimethyl carbonate from carbon dioxide over ceria nanorod catalysts. *J. Catal.* **2016**, *340*, 295–301.
- [11] Tundo, P.; Selva, M. The chemistry of dimethyl carbonate. *Acc. Chem. Res.* **2002**, *35*, 706–716.
- [12] Schifter, I.; González, U.; González-Macias, C. Effects of ethanol, ethyl-tert-butyl ether and dimethyl-carbonate blends with gasoline on SI engine. *Fuel* **2016**, *183*, 253–261.
- [13] Zhang, G. D.; Liu, H.; Xia, X. X.; Zhang, W. G.; Fang, J. H. Effects of dimethyl carbonate fuel additive on diesel engine performances. *Proc. Inst. Mech. Eng. Part D* **2005**, *219*, 897–903.
- [14] Liu, Q.; Wu, L. P.; Jackstell, R.; Beller, M. Using carbon dioxide as a building block in organic synthesis. *Nat. Commun.* **2015**, *6*, 5933.
- [15] Chang, K.; Zhang, H. C.; Cheng, M. J.; Lu, Q. Application of ceria in CO_2 conversion catalysis. *ACS Catal.* **2020**, *10*, 613–631.
- [16] Zhang, M.; Xu, Y. H.; Williams, B. L.; Xiao, M.; Wang, S. J.; Han, D. M.; Sun, L. Y.; Meng, Y. Z. Catalytic materials for direct synthesis of dimethyl carbonate (DMC) from CO_2 . *J. Clean Prod.* **2020**, *279*, 123344.
- [17] Santos, B. A. V.; Silva, V. M. T. M.; Loureiro, J. M.; Rodrigues, A. E. Adsorption of H_2O and dimethyl carbonate at high pressure over zeolite 3A in fixed bed column. *Ind. Eng. Chem. Res.* **2014**, *53*, 2473–2483.
- [18] Bansode, A.; Urakawa, A. Continuous DMC Synthesis from CO_2 and methanol over a CeO_2 catalyst in a fixed bed reactor in the presence of a dehydrating agent. *ACS Catal.* **2014**, *4*, 3877–3880.
- [19] Honda, M.; Tamura, M.; Nakagawa, Y.; Nakao, K.; Suzuki, K.; Tomishige, K. Organic carbonate synthesis from CO_2 and alcohol over CeO_2 with 2-cyanopyridine: Scope and mechanistic studies. *J. Catal.* **2014**, *318*, 95–107.
- [20] Li, C. F.; Zhong, S. H. Study on application of membrane reactor in direct synthesis DMC from CO_2 and CH_3OH over Cu-KF/MgSiO catalyst. *Catal. Today* **2003**, *82*, 83–90.
- [21] Aresta, M.; Dibenedetto, A.; Pastore, C.; Cuocci, C.; Aresta, B.; Cometa, S.; de Giglio, E. Cerium(IV)oxide modification by inclusion of a hetero-atom: A strategy for producing efficient and robust nano-catalysts for methanol carboxylation. *Catal. Today* **2008**, *137*, 125–131.
- [22] Saada, R.; Kellici, S.; Heil T.; Morgan, T.; Saha, B. Greener synthesis of dimethyl carbonate using a novel ceria-zirconia oxide/graphene nanocomposite catalyst. *Appl. Catal. B: Environ.* **2015**, *168–169*: 353–362.
- [23] Shi, Q. Q.; Ping, G. C.; Wang, X. J.; Xu, H.; Li, J. M.; Cui, J. Q.; Abroshan, H.; Ding, H. J.; Li, G. CuO/TiO_2 heterojunction composites: An efficient photocatalyst for selective oxidation of methanol to methyl formate. *J. Mater. Chem. A* **2019**, *7*, 2253–2260.
- [24] Chen, Y. D.; Tang, Q.; Ye, Z. B.; Li, Y.; Yang, Y.; Pu, H. Y.; Li, G. Monolithic $\text{Zn}_x\text{Ce}_{1-x}\text{O}_2$ catalysts for catalytic synthesis of dimethyl carbonate from CO_2 and methanol. *New J. Chem.* **2020**, *44*, 12522–12530.
- [25] Chen, Y. D.; Wang, H.; Qin, Z. X.; Tian, S. L.; Ye, Z. B.; Ye, L.; Abroshan, H.; Li, G. $\text{Ti}_x\text{Ce}_{1-x}\text{O}_2$ nanocomposites: A monolithic catalyst for the direct conversion of carbon dioxide and methanol to dimethyl carbonate. *Green Chem.* **2019**, *21*, 4642–4649.
- [26] Chen, Y. D.; Yang, Y.; Tian, S. L.; Ye, Z. B.; Tang, Q.; Ye, L.; Li, G. Highly effective synthesis of dimethyl carbonate over CuNi alloy nanoparticles @porous organic polymers composite. *Appl. Catal. A: Gen.* **2019**, *587*, 117275.
- [27] Tomašić, V.; Jović, F. State-of-the-art in the monolithic catalysts/reactors. *Appl. Catal. A: Gen.* **2006**, *311*, 112–121.
- [28] Jiang, D.; Wang, W. Z.; Gao, E. P.; Zhang, L.; Sun, S. M. Bismuth-induced integration of solar energy conversion with synergistic low-temperature catalysis in $\text{Ce}_{1-x}\text{Bi}_x\text{O}_{2-\delta}$ nanorods. *J. Phys. Chem. C* **2013**, *117*, 24242–24249.
- [29] Anderson, J. M.; Baiker, A. Exploring catalytic solid/liquid interfaces by *in situ* attenuated total reflection infrared spectroscopy. *Chem. Soc. Rev.* **2010**, *39*, 4571–4584.
- [30] Urakawa, A.; Bürgi, T.; Baiker, A. Sensitivity enhancement and dynamic behavior analysis by modulation excitation spectroscopy: Principle and application in heterogeneous catalysis. *Chem. Eng. Sci.* **2008**, *63*, 4902–4909.

- [31] Blöchl, P. E. Projector Augmented-Wave method. *Phys. Rev. B* **1994**, *50*, 17953–17979.
- [32] Kresse, G.; Furthmüller, J. Efficient iterative schemes for *ab initio* total-energy calculations using a plane-wave basis set. *Phys. Rev. B* **1996**, *54*, 11169–11186.
- [33] Ganduglia-Pirovano, M. V.; da Silva, J. L. F.; Sauer, J. Density-functional calculations of the structure of near-surface oxygen vacancies and electron localization on CeO₂(111). *Phys. Rev. Lett.* **2009**, *102*, 026101.
- [34] Li, H. Y.; Wang, H. F.; Gong, X. Q.; Guo, Y. L.; Guo, Y.; Lu, G. Z.; Hu, P. Multiple configurations of the two excess 4f electrons on defective CeO₂(111): Origin and implications. *Phys. Rev. B* **2009**, *79*, 193401.
- [35] Henkelman, G.; Uberuaga, B. P.; Jónsson, H. A climbing image nudged elastic band method for finding saddle points and minimum energy paths. *J. Chem. Phys.* **2000**, *113*, 9901–9904.
- [36] Chen, A. L.; Zhou, Y.; Ta, N.; Li, Y.; Shen, W. J. Redox properties and catalytic performance of ceria-zirconia nanorods. *Catal. Sci. Technol.* **2015**, *5*, 4184–4192.
- [37] Wang, Z. Q.; Zhang, M. J.; Hu, X. B.; Dravid, V. P.; Xu, Z. N.; Guo, G. C. CeO_{2-x} quantum dots with massive oxygen vacancies as efficient catalysts for the synthesis of dimethyl carbonate. *Chem. Commun.* **2020**, *56*, 403–406.
- [38] Santra, C.; Auroux, A.; Chowdhury, B. Bi doped CeO₂ oxide supported gold nanoparticle catalysts for the aerobic oxidation of alcohols. *RSC Adv.* **2016**, *6*, 45330–45342.
- [39] Shi, Q. Q.; Qin, Z. X.; Yu, C. L.; Waheed, A.; Xu, H.; Gao, Y.; Abroshan, H.; Li, G. Experimental and mechanistic understanding of photo-oxidation of methanol catalyzed by CuO/TiO₂-spindle nanocomposite: Oxygen vacancy engineering. *Nano Res.* **2020**, *13*, 939–946.
- [40] Zheng, J. H.; Jiang, Q.; Lian, J. S. Synthesis and optical properties of flower-like ZnO nanorods by thermal evaporation method. *Appl. Surf. Sci.* **2011**, *257*, 5083–5087.
- [41] Zhang, X. Y.; Qin, J. Q.; Xue, Y. N.; Yu, P. F.; Zhang, B.; Wang, L. M.; Liu, R. P. Effect of aspect ratio and surface defects on the photocatalytic activity of ZnO nanorods. *Sci. Rep.* **2014**, *4*, 4596.
- [42] Li, M. M.; Wang, P. F.; Ji, Z. Z.; Zhou, Z. R.; Xia, Y. G.; Li, Y.; Zhan, S. H. Efficient photocatalytic oxygen activation by oxygen-vacancy-rich CeO₂-based heterojunctions: Synergistic effect of photoexcited electrons transfer and oxygen chemisorption. *Appl. Catal. B: Environ.* **2021**, *289*, 120020.
- [43] Shi, Y. Y.; Tian, S. L.; Shi, Q. Q.; Zhang, Y. F.; Waheed, A.; Cao, Y.; Li, G. Cascade aldol condensation of an aldehyde via the aerobic oxidation of ethanol over an Au/NiO composite. *Nanoscale Adv.* **2019**, *1*, 3654–3659.
- [44] Liu, B.; Li, C. M.; Zhang, G. Q.; Yao, X. S.; Chuang, S. S. C.; Li, Z. Oxygen vacancy promoting dimethyl carbonate synthesis from CO₂ and methanol over Zr-doped CeO₂ nanorods. *ACS Catal.* **2018**, *8*, 10446–10456.
- [45] Turek, A. M.; Wachs, I. E.; DeCanio, E. Acidic properties of alumina-supported metal oxide catalysts: An infrared spectroscopy study. *J. Phys. Chem.* **1992**, *96*, 5000–5007.
- [46] di Cosimo, J. I.; Díez, V. K.; Xu, M.; Iglesia, E.; Apesteguía, C. R. Structure and surface and catalytic properties of Mg-Al basic oxides. *J. Catal.* **1998**, *178*, 499–510.
- [47] Baumgarten, E.; Zachos, A. Infrared spectroscopical investigations on the adsorption of CO₂ on aluminas and silica aluminas at elevated temperatures. *Spectrochim. Acta A* **1981**, *37*, 93–98.
- [48] Dreyer, J. A. H.; Li, P. X.; Zhang, L. H.; Beh, G. K.; Zhang, R. D.; Sit, P. H. L.; Teoh, W. Y. Influence of the oxide support reducibility on the CO₂ methanation over Ru-based catalysts. *Appl. Catal. B: Environ.* **2017**, *219*, 715–726.
- [49] Jung, K. T.; Bell, A. T. An *in situ* infrared study of dimethyl carbonate synthesis from carbon dioxide and methanol over zirconia. *J. Catal.* **2001**, *204*, 339–347.